INVOTEK

Jurnal Inovasi Vokasional dan Teknologi

http://invotek.ppj.unp.ac.id/index.php/invotek

Vol. 25, No. 2, June 2025

ISSN: 1411 – 3411 (p)
ISSN: 2549 – 9815 (e)

Analysis of Air Flow Characteristics on a Savonius Wind Turbin Next to a Building through CFD Simulation

Audha Fitrah Aulina[1] *, Haning Hasbiyati[2]

[1] Automotive Engine Study Program, Department of Engineering, Politeknik Negeri Jember
Jl. Mastrip PO BOX 164, Jember, Indonesia-68101

[2] Renewable Energy Engineering Study Program, Department of Engineering, Politeknik Negeri Jember
Jl. Mastrip PO BOX 164, Jember, Indonesia-68101

*Corresponding author: audha_fitrah@polije.ac.id

Doi: https://doi.org/10.24036/invotek.v25i2.1294

Abstract

Urban environments pose significant challenges for wind energy utilization due to highly complex, non-uniform, and turbulence-dominated airflow around buildings. Although the Savonius vertical-axis turbine is capable of operating under such conditions, its performance remains highly sensitive to installation placement and configuration. This study conducts a two-dimensional CFD investigation to evaluate the aerodynamic behavior of two tandem-arranged Savonius turbines mounted adjacent to a wall. Two blade-orientation configurations are assessed: Configuration 1, where the returning blades face each other, and Configuration 2, where the advancing blades are adjacent. Transient simulations employing a validated CFD framework with the Realizable k-ε turbulence model are performed at a 7 m/s inflow velocity across a range of tip speed ratios. The results reveal pronounced wall–flow interactions characterized by flow deflection and blockage effects. Configuration 2 demonstrates superior aerodynamic performance, achieving a higher maximum power coefficient over a broader TSR range. This improvement is attributed to a favorable "nozzle effect" generated between the advancing blade of the front turbine and the wall, which accelerates the incoming flow toward the rear turbine and enhances its inflow conditions. In contrast, Configuration 1 exhibits stronger wake interference and more severe blockage, particularly at higher TSR values. Overall, the findings indicate that an adjacent advancing-blade arrangement optimizes aerodynamic interaction and energy extraction for wall-mounted tandem Savonius turbines, offering valuable insights for the design of small-scale urban wind energy systems.

Keywords: Savonius Turbine, CFD, Tandem Configuration, Blade Orientation, Aerodynamic Performance.

1. Introduction

Wind energy collection in city zones is extremely hampered by non-uniform wind directions and speeds, as well as strong intensity turbulence caused by buildings, trees, and structures. Literature has shown that urban morphology, such as building height and density, plays an important role in wind speed distribution and wind energy potential, where denser and higher-built cities experience lower wind speeds and higher turbulence [1], [2]. The importance of innovation and optimization of turbine design to increase efficiency and durability [3]. To counter such challenges, novel wind turbine design approaches, such as vertical-axis turbines, building-integrated systems, and targeted designs such as diffuser shrouds, have been suggested to provide improved efficiency under fluctuating urban wind environments [4]–[6].

Deployment of turbines atop skyscrapers and making use of the characteristics of wind flow pattern around buildings has the possibility of increasing the prospects of wind energy. alternative energy and emerging markets remain under-explored [7]. The assessment of sites for installation must be conducted considering accurate microenvironmental parameters derived from CFD simulations and field measurements [8]. Besides, artificial intelligence and machine learning technologies are being used

Received date 08/11/2024, Revised date 03/12/2025, Accepted date 10/12/2025

P-ISSN: 1411-3414
E-ISSN: 2549-9815

more and more to map and predict wind resources in complex urban areas better [4], [9]. Generally speaking, where there is potential for wind energy in urban areas, its efficiency and cost-effectiveness are largely defined by turbine design, optimal placement, and good understanding of local wind patterns [5], [8], [10].

The complex interactions between structures and wind turbines in the urban environment produce highly turbulent and unstable wind flow patterns that induce acceleration and vortex regions that have direct effects on turbine performance. In previous research, it has been shown that buildings are able to reduce downstream wind speeds by significant values and elevate turbulence intensity. Therefore, turbine installation and design must consider local flow patterns in detail [11], [12]. However, the complex mechanisms of this interaction remain not fully explained due to the nature of the flow field around buildings.

Computational Fluid Dynamics (CFD) has been a strong tool to guarantee complete modeling and analysis of wind flow behavior around buildings and turbines, including energy potential measuring, velocity distribution, turbulence, and the optimal placement of turbine installations [12]–[14]. Simulation results show that increasing the inlet velocity results in a more turbulent flow [15]. CFD can be employed to verify simulation outputs against field data, and to develop building or turbine designs that are capable of increasing wind speed and reducing turbulence, for example, by using rounded rooflines or integrating turbines into buildings [14]. However, the cross-cutting concerns in CFD applications include the selection of turbulence model, meshing and domain configuration, and expensive computations. Consequently, methodologies and optimal practices remain [13], [16].

Airflow conditions around buildings are normally highly non-uniform and complex due to the rolling, recirculation, and high turbulence effects of the wake. Such flow patterns significantly influence the aerodynamic efficiency of wind turbines, especially vertical-axis types like Savonius turbines, that are normally utilized in low-speed regions and locations with fluctuating directions of flow. To visualize wind behavior in such conditions, this study will utilize computer simulations through Computational Fluid Dynamics (CFD). With this, the airflow performance around the building and turbine can be "visualized" in detail, that is, the velocity, pressure, and turbulence patterns affecting turbine performance. The principal concern of this study is collecting pertinent numerical values to account for the flow behavior and how these are tied with the dynamic performance of the turbine.

Some previous research have found that dynamic torque in a turbine is significantly influenced by flow fluctuations caused by turbulence. A rise in turbulence intensity can lead to higher fluctuations in torque and increase dynamic loading on the turbine structure [17]–[19]. Conversely, the static torque, which determines the initial ability of the turbine to rotate, is further controlled by blade shape and flow conditions in a localized area, although turbulence still has the dominant role among the dynamic characteristics [17], [18].

More turbulence intensity around a turbine has also been found to increase the power coefficient up to 22% in small-scale vertical-axis turbines with turbulence intensity increased from 0.7% to 20% [20], [21]. This effect is smaller for large-scale turbines due to fluctuating flow scales and distribution of kinetic energy. Besides, pressure coefficient distribution along the blade surface and structure mapping of construction structures shows that the increased turbulence intensity amplifies pressure fluctuations, and thus bigger aerodynamic loads as well as the risk of structural vibration [22].

Numerical and experimental research also confirm that the negative and positive pressure distribution on the blade surface is a dominant parameter in the development of torque and rotational efficiency of the turbine [22]. Turbulence intensity, pressure distribution pattern, and flow velocity are highly relevant in determining the flow characteristics around a Savonius turbine placed next to a building. Turbulence intensity is a useful measurement because high-intensity flow disturbances can cause aerodynamic loading instability on the turbine blades, which directly reduces efficiency and creates vibrations. Therefore, mapping the pressure coefficient on the turbine blade surface is necessary, a factor closely related to the distribution of aerodynamic forces that ultimately cause possible turbine vibrations, as obtained by [23], [24]. In this regard, CFD studies revealed that placing the turbine at the edge or corner of a building can increase the wind speed and subsequently increase the turbulence intensity, thus causing a significant increase in Cp in the Savonius turbine, up to 92.5%, in contrast to uniform flow field conditions, as presented in [25], [26] However, the resulting increase in turbulence can cause fluctuations in torque and load on the turbine and thus must be taken into consideration when determining the turbine position and orientation, as demonstrated by [27], [28]. It can be seen that the

combination of analysis on turbulence intensity, pressure distribution, and flow velocity patterns through CFD can provide one with a comprehensive picture of the flow characteristics around a Savonius turbine. From the obtained results, one important basis is provided on which the most appropriate turbine position and orientation can be determined to optimally and efficiently exploit the full potential for urban wind energy, as seen in previous studies by [25], [26], [28].

Despite extensive research on the potential use of wind energy in urban areas, a thorough understanding of the interactions between flow velocity, turbulence intensity, and pressure distribution in Savonius turbines near buildings remains lacking. Previous studies have often examined these parameters separately, and detailed CFD visualizations of wake behavior, vortex formation, and their effects on torque fluctuations and aerodynamic loads are lacking. Furthermore, traditional CFD methods are inadequate for accurately simulating complex micro-urban wind conditions and identifying the most suitable turbine locations. This study aims to address this gap by introducing an integrated CFD analysis. This analysis links velocity patterns, turbulence levels, and pressure coefficients. It also provides a more detailed aerodynamic mapping of the building-turbine system. Consequently, this study provides new insights into the flow characteristics around Savonius turbines in urban environments and helps develop more effective turbine placement strategies.

2. Material and Method

2.1 Design and Computational Domain

The Savonius wind turbine features two distinct blade types according to wind direction: the concave side (advancing blade) and the convex side (returning blade) [29]. This research examines the influence of the nearest blade sides on two tandem-configured Savonius wind turbines mounted next to a wall on one side. The study looks at two setups: configuration 1, where the returning blades are next to each other, and configuration 2, where the advancing blades are next to each other. In configuration 1, the front turbine rotates counterclockwise, while the rear turbine rotates clockwise. In configuration 2, the front turbine rotates clockwise, while the rear turbine rotates counterclockwise. This study illustrates the concept and geometry in Figure 1.

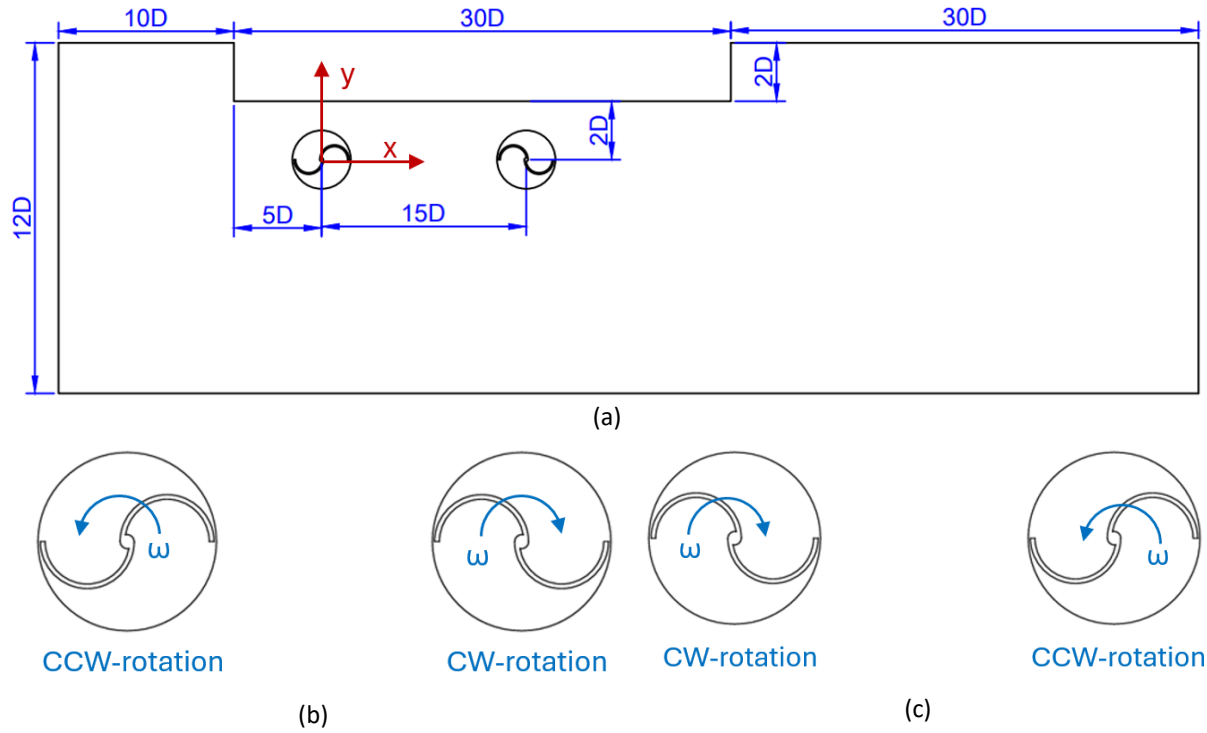

Figure 1. Research Configurations: a) Overall Design and Geometry, b) Configuration 1, c) Configuration 2

This study used a conventional Savonius wind turbine featuring a semi-circular blade type, with a blade diameter (D) of 500 mm, a rotor diameter (L) of 940 mm, an endplate diameter (Do) of 1000 mm, a shaft diameter (b) of 60 mm, and a blade thickness (x) of 25 mm. The height of the turbine can

P-ISSN: 1411-3414
E-ISSN: 2549-9815

be ignored in this study because it uses two-dimensional modeling [30]. he configuration of the Savonius wind turbine in this research is illustrated in Figure 2.

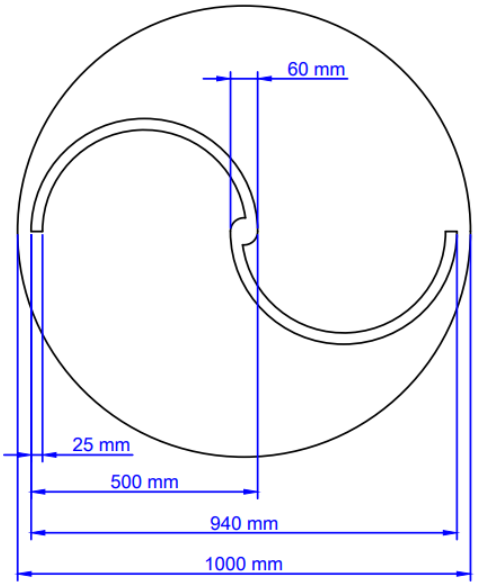

Figure 2. Schematic Diagram of the Savonius Wind Turbine

The computational domain is separated into two parts: the rotating domain and the stationary domain [31], as shown in Figure 3. The rotating domain contains the rotor, which rotates throughout the simulation and requires a high-quality mesh [32]. The stationary domain, including the inlet wall, interface, and outlet, remains fixed and maintains a constant velocity throughout the simulation procedure [33]. In this research, the dimensions of the interface boundary condition correspond to the endplate diameter, and the domain type and size are modified according to previous studies [34].

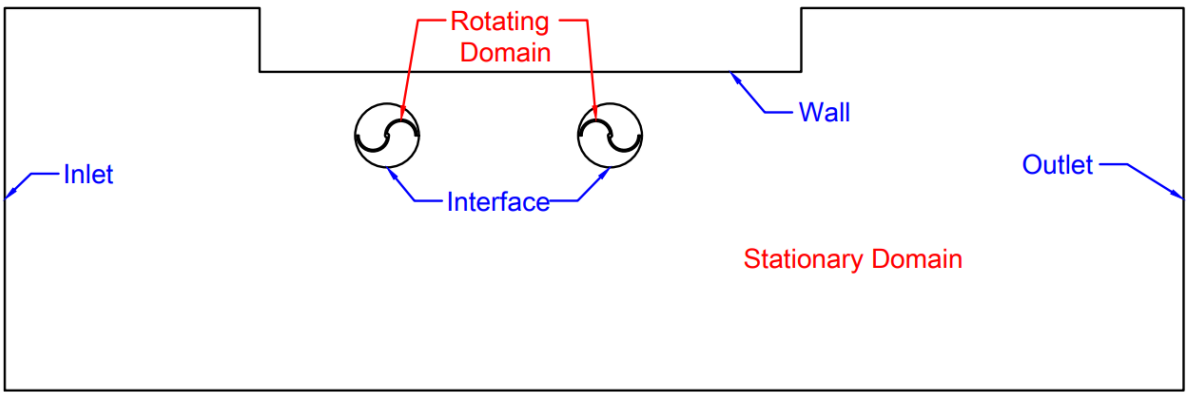

Figure 3. Computational domain

2.2 Mesh Generation and Grid Independence Test

The mesh generated consists of both a structured mesh and an unstructured mesh, as shown in Figure 4. The structured mesh is created in the stationary domain using supporting lines. The unstructured mesh is generated in the rotating domain region as a result of inflation layers around the turbine blade. Inflation layers are used to precisely compute the flow field around the blade [35]. The inflation layers used consist of a first layer thickness of 0.1 mm, a maximum of 15 layers, and a growth rate of 1.2. A mesh qualifies as good when it satisfies the conditions of maximum skewness < 0.95 and minimum orthogonal quality > 0.1 [36]. In this study, the maximum skewness was found to be 0.6 and the minimum orthogonal quality was 0.2. Therefore, it can be said that the mesh formed is already good.

P-ISSN: 1411-3414
E-ISSN: 2549-9815

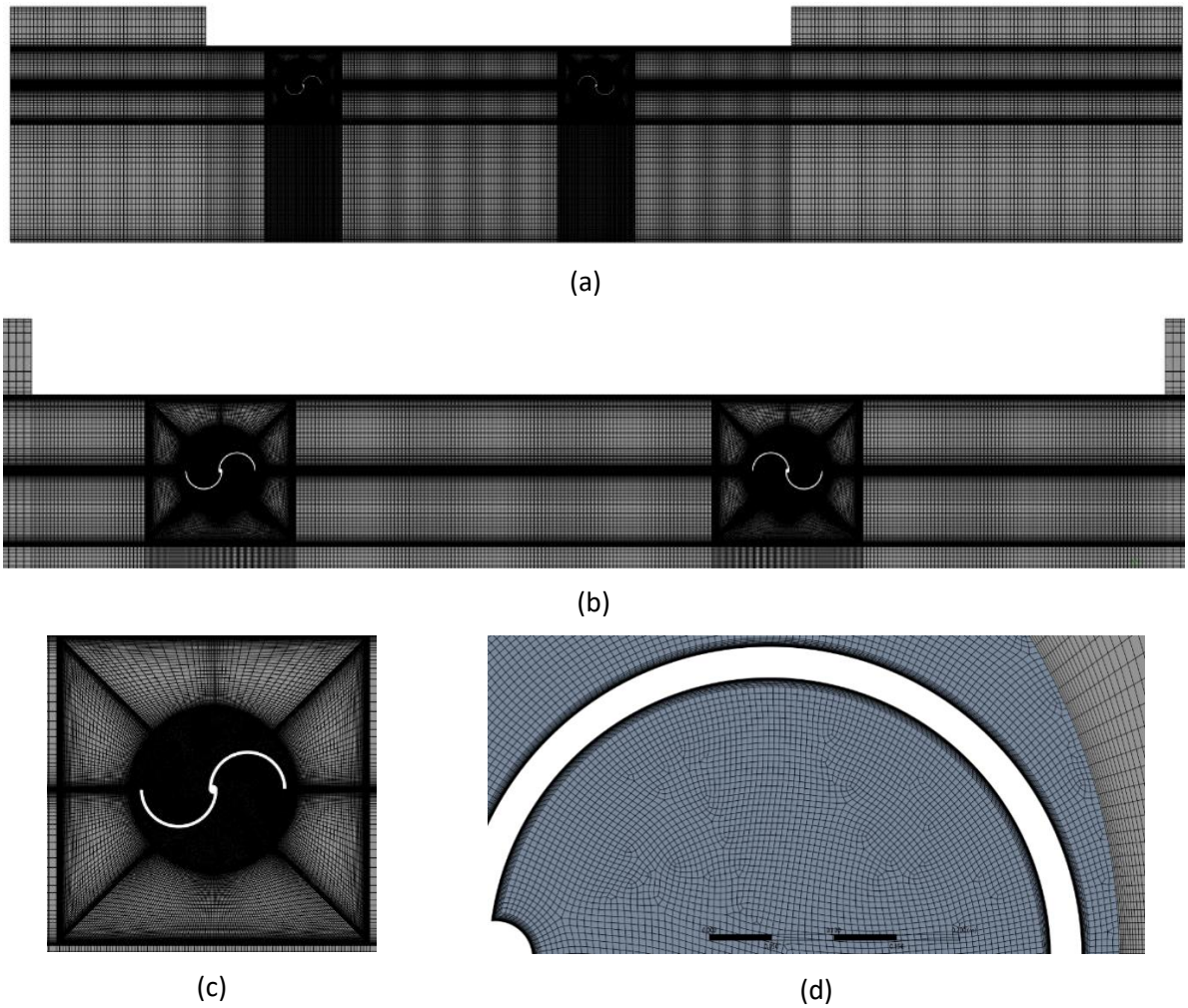

Figure 4. Meshing Generation: a) All Domain, b) Adjacent Wall and Turbines, c) Single Turbine, d) Blade

A grid independence test is required to examine the effect of varying the number of elements on the final parameters while also avoiding unnecessarily extended simulation durations [37]. The grid independence test is conducted by varying the number of mesh elements while maintaining the same solver configuration. The number of mesh elements selected corresponds to the number at which the results demonstrate convergence and do not exhibit significant inaccuracies.

The number of mesh elements in the grid independence test varied from 50,000 to 160,000 at a tip speed ratio of 1 under no-wall conditions. Table 1 shows that the moment coefficient values became stable at 75,000 elements, with the corresponding error consistently remaining below 5% as the number of elements increased. The graph illustrating the moment coefficient as a function of the azimuth angle (Figure 5) indicates that at approximately 75,000 elements, the curves converge, demonstrating minimal variation in the moment coefficient values.

Table 1. Grid Independence Test Result

Elements	Tip Speed Ratio	Moment Coefficient	Error (%)
50,000	1	0.08620	-
75,000	1	0.07385	16.72333
110,000	1	0.07193	2.663875
130,000	1	0.07163	0.42518
160,000	1	0.07157	0.08156

P-ISSN: 1411-3414
E-ISSN: 2549-9815

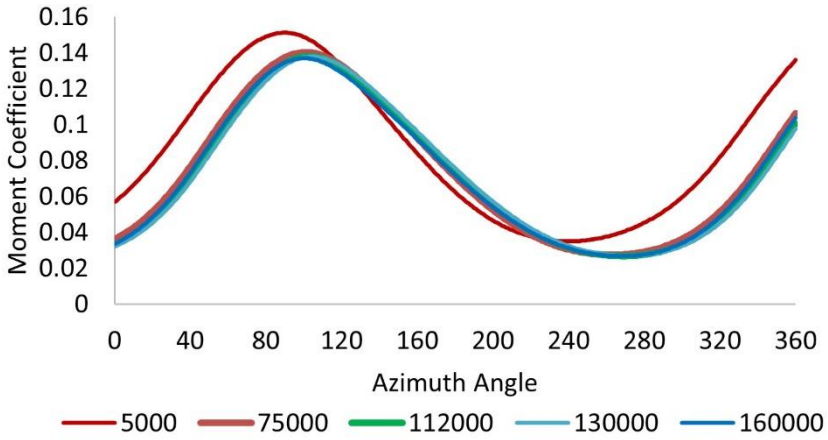

Figure 5. Graph of the Moment Coefficient as a Function of Azimuth Angle for Different Mesh Element Numbers

2.3 Boundary Conditions

Boundary conditions represent the simulation domain and conditions corresponding to the actual physical situation. In this study, the applied boundary conditions consist of an inlet, outlet, wall, and rotor. At the inlet, a uniform flow condition is assumed with a wind velocity of 7 m/s, a turbulence intensity of 3%, and a turbulence length scale of 66 mm to represent the upstream conditions. The outlet, representing the downstream region, is defined as a pressure outlet with a gauge pressure of 0 Pa. The wall boundary is assigned to a no-slip condition. In the rotor region, a no-slip and moving wall condition is applied, with the rotational speed adjusted according to the cell zone condition in the rotating domain.

2.4 Solver Setup

The airflow around the rotor exhibits a high Reynolds number, indicating that the flow in this region is turbulent. In general, solving turbulent flow problems is challenging due to the irregular, diffusive, and dissipative nature of the flow. Therefore, turbulence modeling is required to accurately simulate such complex flow behavior. A commonly used approach for modeling turbulence is the Reynolds-Averaged Navier–Stokes (RANS) method, which includes the Spalart–Allmaras model, the turbulent kinetic energy–dissipation rate model (k–ε model), and the turbulent kinetic energy–specific dissipation rate model (k–ω model). In this study, the realizable k–ε model with enhanced wall treatment was employed. This model was selected because the combination of the realizable k–ε formulation and enhanced wall treatment provides better accuracy and faster computational convergence compared to other turbulence models [38].

Table 2. Time Step Size based on Tip Speed Ratio

TSR	V (m/s)	ω (rad/s)	Time Step Size
0.2	7	2.979	0.005856
0.4	7	5.957	0.002928
0.6	7	8.936	0.001952
0.8	7	11.915	0.001464
1.0	7	14.894	0.001171
1.2	7	17.872	0.000976
1.4	7	20.851	0.000837
1.6	7	23.830	0.000732
1.8	7	26.809	0.000651
2.0	7	29.787	0.000586
2.2	7	32.766	0.000532

P-ISSN: 1411-3414
E-ISSN: 2549-9815

The rotating domain region was defined in the cell zone condition setting using the mesh motion approach [39] where the rotor's angular velocity (ω) depends on the tip speed ratio (TSR) and the upstream wind velocity. The TSR is closely related to both the power coefficient and the moment coefficient, as expressed in the following equations:

$$TSR = \frac{\omega \,.\, R}{v} \quad (1)$$

where ω is the angular velocity, v is the flow velocity, and R is the turbine radius, which can be determined using:

$$R = 2D - \frac{b}{2} \quad (2)$$

Accordingly, the moment coefficient (Cm) and power coefficient (Cp) can be defined as:

$$Cm = \frac{T}{\frac{1}{2} \,.\, \rho \,.\, A \,.R \,.V^2} \quad (3)$$

$$Cp = Cm \times TSR \quad (4)$$

In transient numerical modeling, the time step size represents the time required for the turbine to rotate by 1º [40]. The time step size values used in this study are presented in Table 2, and the complete solver setup is described in the subsequent section. The determination of the time step size is governed by the turbine's rotational speed (N) and the azimuth angle or degree of rotation per time step (θ) as expressed by the following equation:

$$TSS = \frac{60}{N} \times \frac{\theta}{360} \quad (6)$$

The solver setup used in this simulation is shown in Table 3 as follows:

Table 3. Solver setup

Parameters		Input
General	Solver	2D Planar; Pressure-based; Transient
Models	Viscous	k-epsilon; Realizable; Enhanced wall treatment
Materials	Air	ρ = 1.176 kg/m^3; μ = 1.851× 10^{-5} kg/m.s
Cell Zone Condition	Rotating zone domain	Air; Mesh motion; Turbine rotation speed (rad/s)
	Stationary zone domain	Air
Boundary Condition	Inlet	Inlet velocity = 7 m/s; Turbulence intensity = 3%; Turbulence length scale = 66 mm
	Outlet	Pressure outlet; P = 0 Pa
	Wall	Wall; No slip
	Rotor	Moving wall; Rotational; No slip
	Mesh interface	Interface 1; Interface 2
Reference Values	Area (m^2)	0.94
	Density (kg.m^3)	1.176
	Depth (m)	1
	Enthalpy (J/kg)	0
	Length (m)	0.47
	Pressure (Pa)	0
	Temperature (K)	301.15
	Velocity (m/s)	7
	Viscosity (kg/m.s)	1.851× 10^{-5}
	The ratio of specific heats	1
	Yplus for heat trans. Coef.	300
Solution	Methods	Scheme; SIMPLE

P-ISSN: 1411-3414
E-ISSN: 2549-9815

	Gradient; Least square cell-based
	Pressure; Second order upwind
	Momentum; Second order upwind
	Turbulence kinetic energy; Second order upwind
	Turbulence dissipation rate; Second order upwind
Control	Residual; Absolute criteria 10^{-5}
Calculation	Number of time steps = 3600; Max iteration = 100; The time step size can be seen in Table 2

To verify the reliability and accuracy of the solver setup, a validation process was performed by comparing the present numerical results with those from previous research under identical Reynolds number conditions. The study reported in [40] served as the benchmark, corresponding to a single-turbine configuration without a wall and a Reynolds number of 140,000. As depicted in Figure 6 the moment coefficient values obtained in the present work exhibit strong agreement with those reported by [40], with discrepancies across all tip speed ratios remaining below 5%. These findings confirm that the solver setup employed in this study is appropriately validated and capable of accurately representing the physical behavior of the flow field.

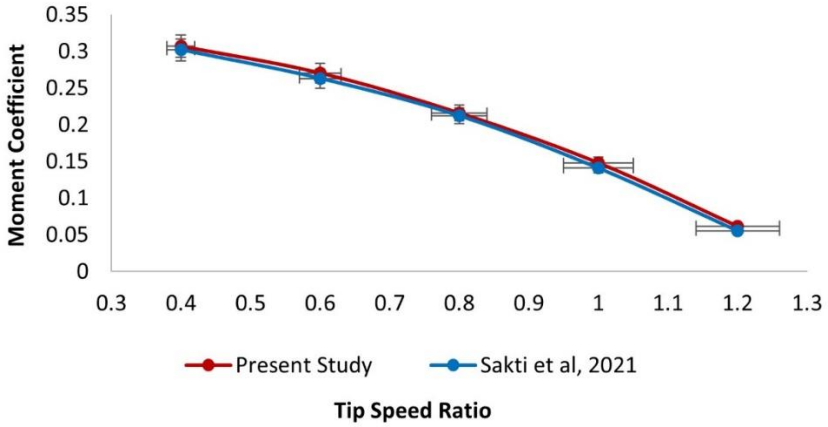

Figure 6. Validation Process Result Graph

3. Result and Discussion

3.1 The Effect of Adjacent Returning Blades (Configuration 1)

3.1.1 Moment Coefficient dan Power Coefficient

The presence of the wall influences the incoming flow by causing a deflection away from the wall, which results from the formation of a bubble separation phenomenon near the wall edge [41], [42]. This interaction leads to the development of a low-velocity region around the wall boundary. The low-velocity region forms near the convex side of the returning blade of the fore turbine, resulting in a higher maximum moment coefficient for the fore turbine compared to the rear turbine at a tip speed ratio of 0.8 Figure 7 However, as shown in the power coefficient distribution Figure 8 the maximum power coefficient is attained by the rear turbine at a tip speed ratio of 1.2. Nevertheless, at a tip speed ratio of 0.8, the fore turbine still exhibits a higher power coefficient than the rear turbine. As the tip speed ratio increases further, both the moment and power coefficients of the fore turbine decrease after reaching their respective peak values. This phenomenon can be attributed to the intensified blockage effect that occurs with increasing turbine rotational speed.

The presence of the wall influences the incoming flow by causing a deflection away from the wall, which results from the formation of a bubble separation phenomenon near the wall edge [41], [42]. This interaction leads to the development of a low-velocity region around the wall boundary. The low-velocity region forms near the convex side of the returning blade of the fore turbine, resulting in a higher maximum moment coefficient for the fore turbine compared to the rear turbine at a tip speed ratio of 0.8

Figure 7. However, as shown in the power coefficient distribution Figure 8 the maximum power coefficient is attained by the rear turbine at a tip speed ratio of 1.2. Nevertheless, at a tip speed ratio of 0.8, the fore turbine still exhibits a higher power coefficient than the rear turbine. As the tip speed ratio increases further, both the moment and power coefficients of the fore turbine decrease after reaching their respective peak values. This phenomenon can be attributed to the intensified blockage effect that occurs with increasing turbine rotational speed.

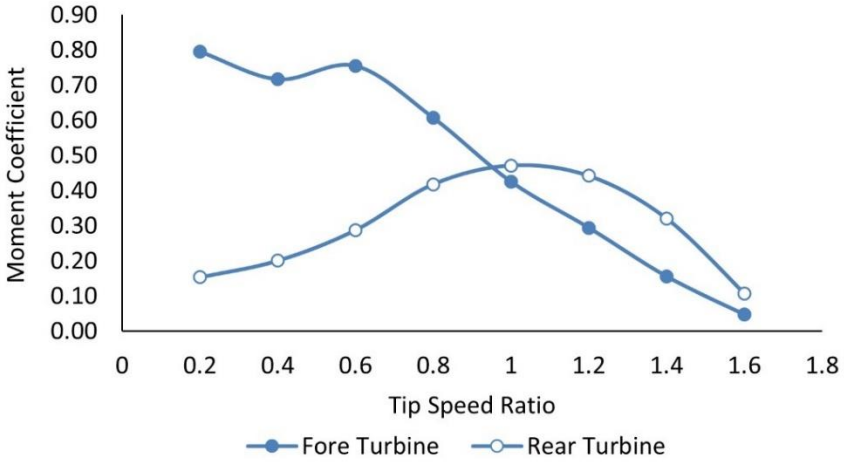

Figure 7 Moment Coefficient as a Function of Tip Speed Ratio Graph for Configuration 1

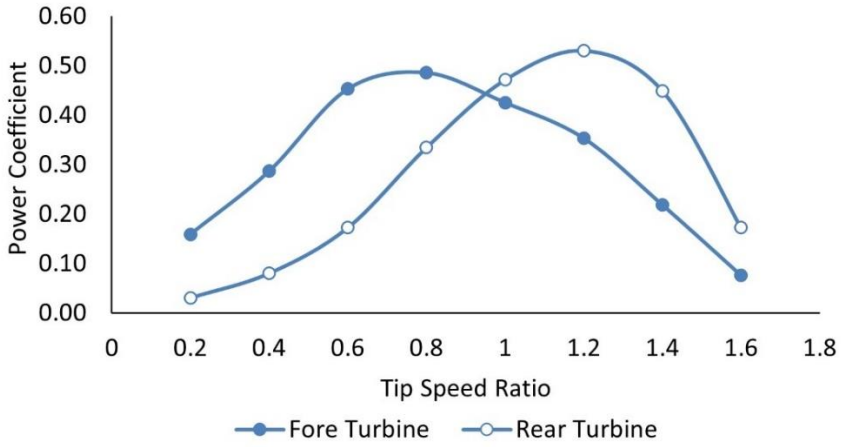

Figure 8. Power Coefficient as a Function of Tip Speed Ratio Graph for Configuration 1

The rear turbine operates within the wake region generated by the fore turbine, resulting in significantly lower moment and power coefficients for the rear turbine at low tip speed ratios (TSR < 1). As the tip speed ratio increases ($1 \leq TSR \leq 1.6$), the rear turbine begins to receive part of the deflected flow from the fore turbine. Consequently, a nozzle effect develops on the concave side of the advancing blade of the rear turbine, leading to higher moment and power coefficients compared to the fore turbine. However, as the nozzle effect between the wall and the advancing blade of the rear turbine becomes stronger, the blockage effect also intensifies. This increased blockage effect ultimately causes both the moment coefficient and the power coefficient to decrease after reaching their peak values.

3.1.2 Velocity and Pressure Contour

The velocity contours of the fore and rear turbines for configuration 1 at an azimuth angle of 90° are presented in Figure 9. The upstream flow impinges on the wall, generating a large vortex near the wall edge and producing a high-velocity region above it. Part of this accelerated flow passes through the gap between the vortex and the convex surface of the returning blade, while the majority impacts the tip of the advancing blade [43]. This interaction drives the fore turbine to rotate counterclockwise (CCW-rotation). A secondary vortex forms near the concave surface of the returning blade due to flow separation at the blade tip, where the adverse pressure gradient intensifies as a result of blade interaction.

P-ISSN: 1411-3414
E-ISSN: 2549-9815

Furthermore, the close proximity of the wall enhances the blockage effect, causing the flow to deviate downward. As the tip speed ratio increases, this blockage effect strengthens, deflecting more of the high-velocity flow downward and leading to the formation of a bubble separation region downstream of the fore turbine.

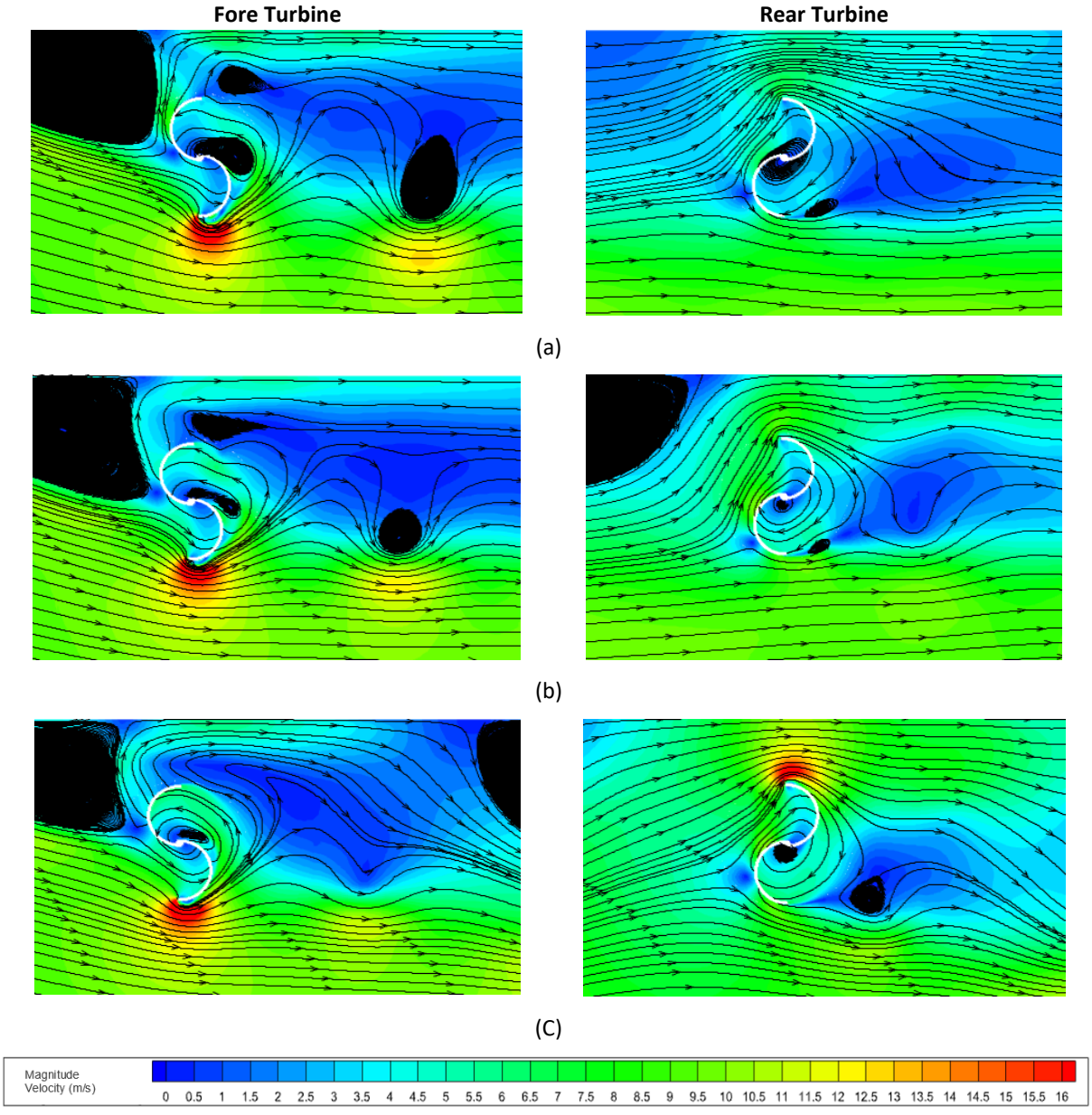

Figure 9. Velocity Contours of the Fore and Rear Turbines for Configuration 1 at an Azimuth Angle of 90°: a) TSR = 0.8, b) TSR = 1.0, c) TSR = 1.2

As shown in Figure 9b, the bubble separation region shifts slightly away from the fore turbine but becomes closely aligned with the advancing blade of the rear turbine. The combined influence of reattached flow and blockage effect gives rise to a nozzle effect, characterized by high-velocity flow between the wall and the advancing blade of the rear turbine. With increasing tip speed ratio Figure 9c, the bubble separation region moves closer to the fore turbine, while the nozzle effect intensifies, resulting in the rear turbine achieving its peak performance at a tip speed ratio of 1.2.

At TSR = 0.8 Figure 10a, a distinct pressure difference is observed between the advancing and returning blades of the fore turbine. A low-pressure zone forms on the advancing blade, while a high-pressure zone develops along the returning blade. The wall induces a localized low-pressure bubble near the tip of the returning blade. Meanwhile, the rear turbine displays a more uniform pressure distribution

P-ISSN: 1411-3414
E-ISSN: 2549-9815

with a lower pressure gradient, leading to lower aerodynamic performance than the fore turbine at this condition.

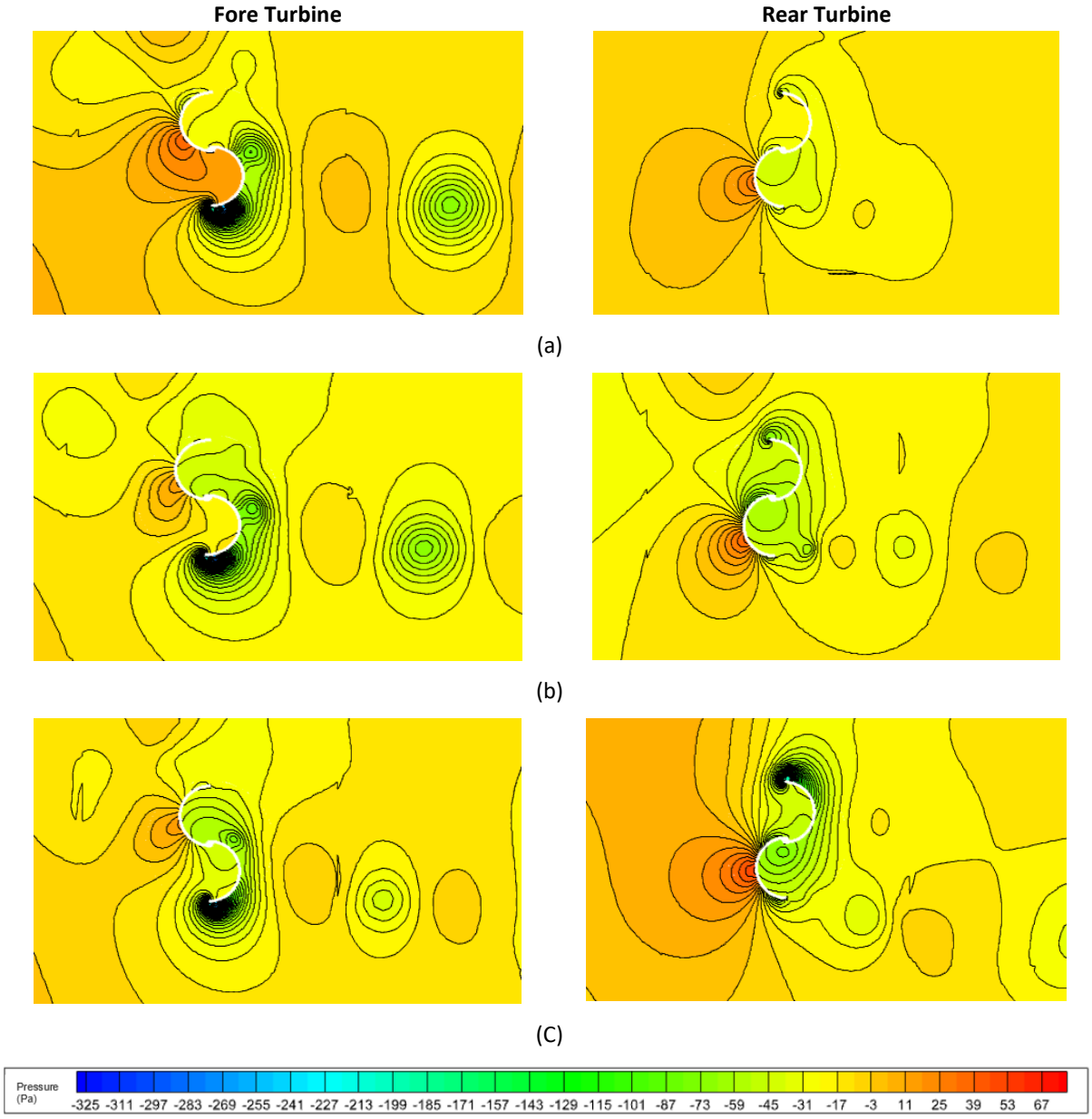

Figure 10. Pressure Contours of the Fore and Rear Turbines for Configuration 1 at an Azimuth Angle of 90°: a) TSR = 0.8, b) TSR = 1.0, c) TSR = 1.2

At TSR = 1 Figure 10b, the pressure variation around the fore turbine becomes more pronounced, indicating a stronger interaction between the primary flow and the vortices generated by the returning blade. Although the bubble separation near the wall persists, it extends further downstream, causing an asymmetric flow pattern around the rear turbine. The side facing the wall experiences elevated pressure, while the opposite side encounters higher flow velocity, signifying significant wake interference from the fore turbine. As TSR increases, the pressure gradient and vortex intensity around both turbines grows stronger. The wall significantly influences the formation of flow deflection and bubble separation patterns, which directly affect the aerodynamic performance of the rear turbine.

At TSR = 1.2 Figure 10c, the pressure gradient surrounding the fore turbine increases sharply, reflecting stronger vortex activity due to higher relative blade velocity. The low-pressure region on the advancing blade becomes more distinct and extends farther downstream, subjecting the rear turbine to a turbulent flow field with considerable pressure fluctuations. However, the wall on the upper side helps

redirect part of the flow downward, slightly shifting the low-pressure zone around the rear turbine away from the wall.

3.2 The Effect of Adjacent Advancing Blades (Configuration 2)

3.2.1 Moment Coefficient dan Power Coefficient

The presence of the wall induces flow separation, leading to the formation of a large vortex region along the wall boundary. In addition, the proximity of the fore turbine to the wall enhances the blockage effect [44], [45]. The interaction of these two phenomena produces a nozzle effect between the concave side of the advancing blade and the wall. Consequently, within the lower tip speed ratio range ($0.2 \leq TSR < 1.6$), the fore turbine exhibits higher moment and power coefficients Figure 11 dan Figure 12 than the rear turbine. However, as the tip speed ratio increases ($TSR \geq 1.6$), the intensified blockage effect significantly reduces the performance of the fore turbine compared with the rear turbine.

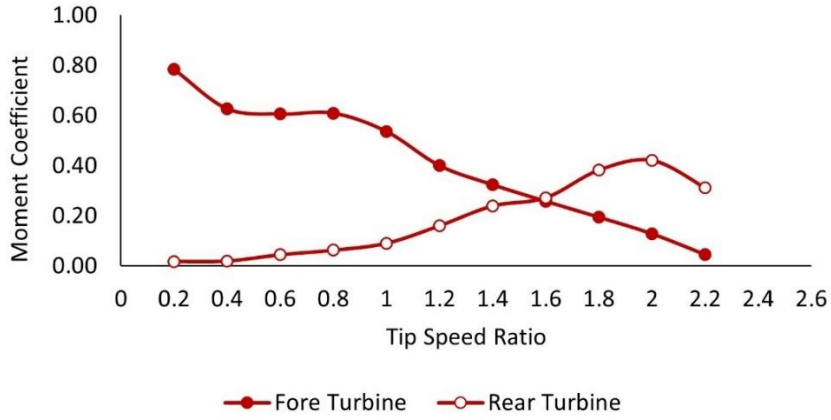

Figure 11. Moment Coefficient as a Function of Tip Speed Ratio Graph for Configuration 2

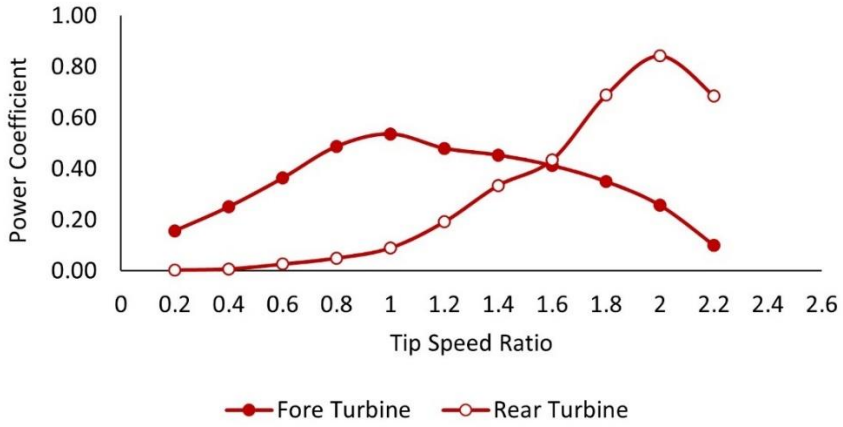

Figure 12. Power Coefficient as a Function of Tip Speed Ratio Graph for Configuration 2

The opposite trend is observed for the rear turbine. At lower tip speed ratios ($0.2 \leq TSR < 1.6$), the rear turbine operates within the wake region generated by the fore turbine, resulting in lower performance compared to the fore turbine. However, as the tip speed ratio increases ($TSR \geq 1.6$), the intensified nozzle effect around the fore turbine constricts the wake region, allowing the concave side of the advancing blade of the rear turbine to experience a relatively higher flow velocity. Consequently, the operational tip speed ratio range of the rear turbine is broader than that of the fore turbine, and its performance becomes more effective at higher tip speed ratios.

3.2.2 Velocity and Pressure Contour

Figure 13 illustrates the velocity contour of the fore and rear turbines for Configuration 2 at an azimuth angle of 90°. The incoming flow strikes the wall edge and subsequently separates, forming a vortex region directly in front of the fore turbine. The separation point occurs on the convex side of the

P-ISSN: 1411-3414
E-ISSN: 2549-9815

returning blade, causing the flow to deflect toward the concave side of the advancing blade. This phenomenon induces a high-velocity region within the narrow gap between the advancing blade and the wall, commonly referred to as the nozzle effect.

At TSR = 1 (Figure 13a), a high-velocity region develops around the advancing blade and slightly affects the convex side of the returning blade. A wake region is also observed downstream of the fore turbine. When the TSR increases to 1.2 (Figure 13b), the high-velocity region around the advancing blade becomes narrower, while the wake region behind the fore turbine extends further downstream. At TSR = 2 (Figure 13c), the high-velocity region becomes wider and increasingly impinges on the convex side of the returning blade. This behavior indicates that the blockage effect acting on the fore turbine intensifies with increasing tip speed ratio. Therefore, it can be concluded that the fore turbine operates more effectively at relatively low tip speed ratio.

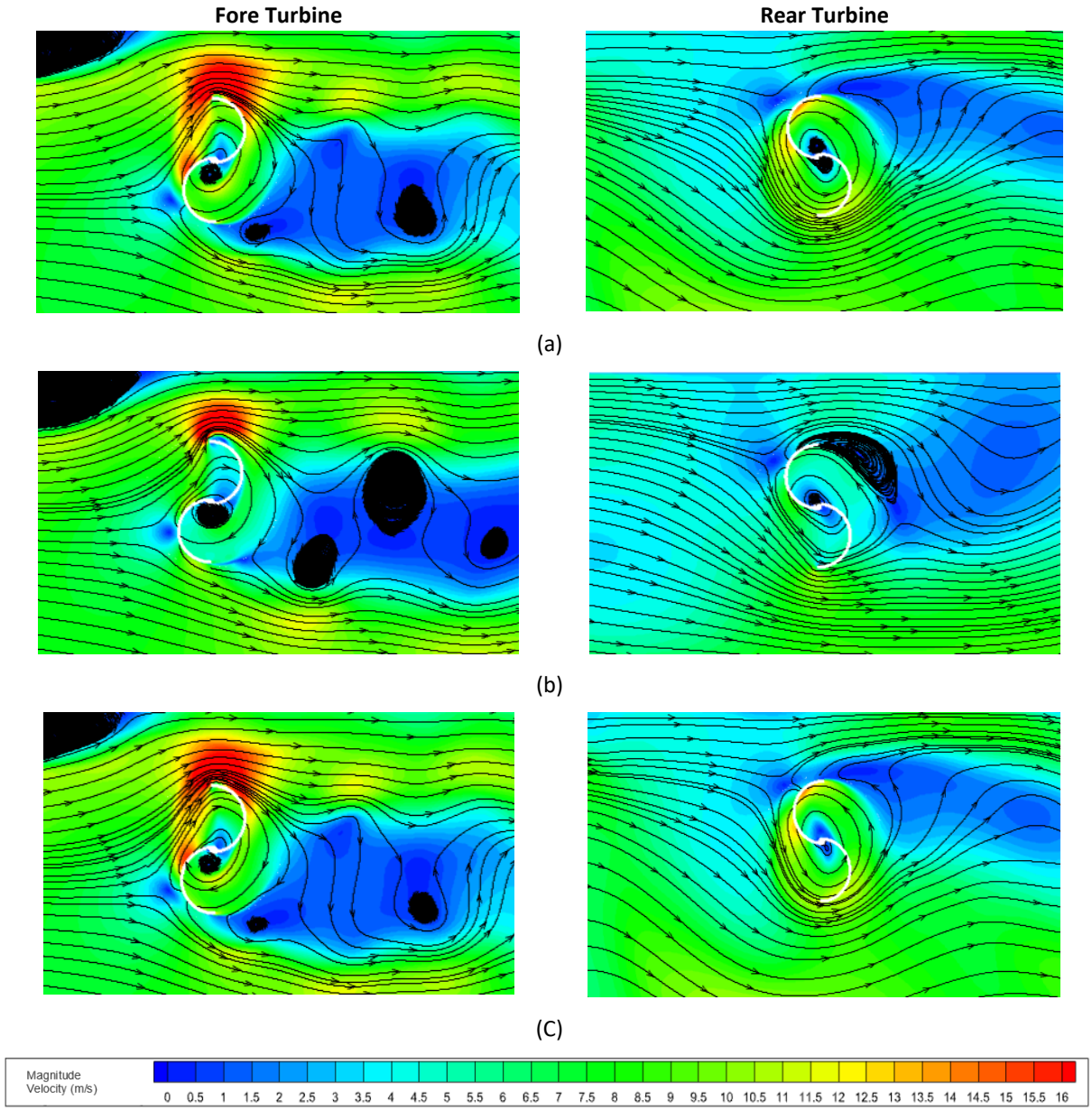

Figure 13. Velocity Contours of the Fore and Rear Turbines for Configuration 2 at an Azimuth Angle of 90°: a) TSR = 1.0, b) TSR = 1.2, c) TSR = 2.0

The rear turbine receives a reduced-velocity flow due to the wake generated by the fore turbine. As a result, the incoming flow on the advancing blade is insufficient to produce significant acceleration, while a strong vortex region forms on the returning blade side due to pronounced flow separation. Increasing the tip speed ratio enhances flow recovery between the two turbines, thereby mitigating the

P-ISSN: 1411-3414
E-ISSN: 2549-9815

wake effect induced by the fore turbine. However, a higher tip speed ratio also intensifies the blockage effect on the rear turbine, which consequently causes a reduction in turbine performance once the optimal operating condition is exceeded.

Figure 14 illustrates the pressure contours of the fore and rear turbines in configuration 2 at an azimuth angle of 90°. Across all TSR variations, the fore turbine experiences a pronounced pressure difference between the advancing and returning blades. The advancing blade, which faces the incoming flow directly, is exposed to a high-pressure region, whereas a low-pressure region develops along the returning blade due to flow separation near the wall and vortex formation. This pressure differential acts as the principal driver of the turbine's torque generation. The proximity of the wall enhances flow deflection, further increasing pressure concentration around the advancing blade, particularly at lower TSRs.

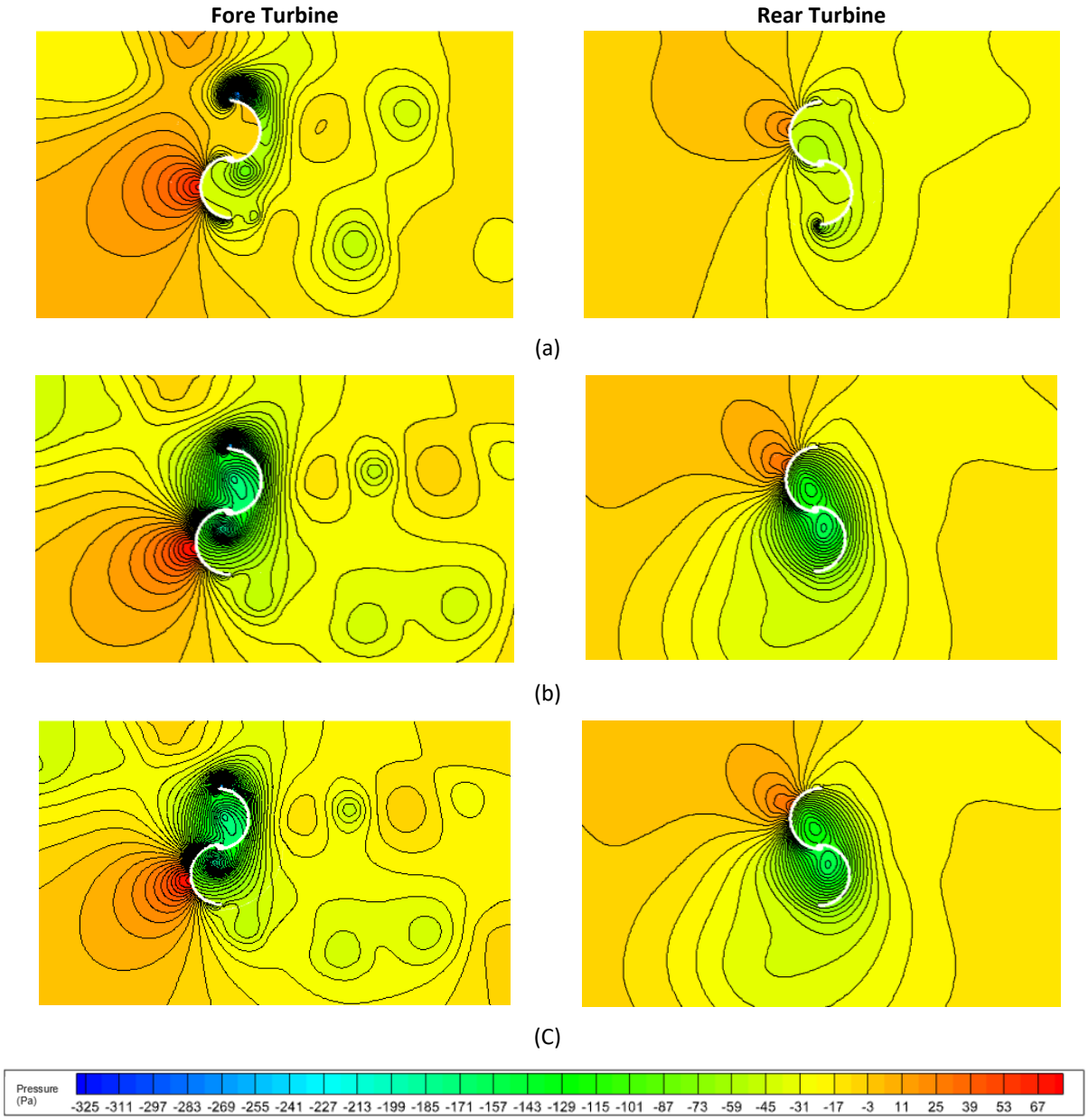

Figure 14. Pressure Contours of the Fore and Rear Turbines for Configuration 2 at an Azimuth Angle of 90°: a) TSR = 1.0, b) TSR = 1.2, c) TSR = 2.0

Meanwhile, the rear turbine's pressure distribution is strongly influenced by the wake generated by the fore turbine. At TSR = 1 Figure 14a, the upstream flow to the rear turbine has lost much of its kinetic energy, resulting in a reduced pressure gradient around the blades. This condition is characterized by relatively uniform pressure distribution and low-pressure regions near the front side of the turbine,

which correspond to decreased torque production. When the TSR increases to 1.2 Figure 14b, both turbines display a more stable pressure pattern. For the fore turbine, the reduced pressure gradient indicates a more stable flow interaction and diminished separation, resulting in a more streamlined outflow toward the rear turbine. Consequently, the rear turbine begins to experience a more balanced pressure distribution, with a high-pressure region forming along its advancing blade.

At TSR = 2 Figure 14c, the pressure distribution around both turbines become more uniform and symmetrical. The fore turbine exhibits a more even pressure spread, while the rear turbine benefits from a partially recovered flow with an increased pressure gradient. This observation suggests that increasing TSR improves inter-turbine interaction by reducing the wake effect and enhancing pressure recovery between the two turbines.

3.3 Comparison between Configuration 1 and Configuration 2

3.3.1 Fore Turbine

Figure 15 illustrates the moment coefficient graph, while Figure 16 presents the power coefficient for both configurations of the fore turbine. At low tip speed ratios (TSR < 1), configuration 1—where the returning blade is positioned closer to the wall—exhibits superior performance compared to configuration 2. The close proximity of the returning blade to the wall induces a low-velocity region caused by flow deflection and bubble separation along the wall boundary. This phenomenon produces a significant pressure gradient between the advancing and returning sides of the blade, resulting in a higher moment coefficient at lower TSR values. However, as the TSR increases, the influence of the wall-induced blockage effect becomes more dominant, elevating the pressure around the blade and consequently reducing turbine performance.

At higher tip speed ratios, configuration 2—where the advancing blade is positioned adjacent to the wall—demonstrates superior aerodynamic performance and achieves the highest maximum coefficient values among both configurations. Moreover, configuration 2 exhibits a wider operational TSR range, indicating better adaptability to higher flow velocities. The proximity of the advancing blade to the wall generates a distinct nozzle effect within the narrow gap between the blade and the wall. The accelerated airflow through this confined region enhances the thrust on the advancing blade, thereby increasing the power coefficient at moderate TSR values. Nonetheless, as the TSR continues to rise, the nozzle effect transitions into a blockage effect, resulting in increased downstream pressure and a subsequent decline in overall performance.

Based on these findings, it can be concluded that the fore turbine in configuration 2 delivers the most optimal performance. This is attributed to its broader operational TSR range and higher maximum power coefficient compared to configuration 1, signifying improved efficiency and adaptability across varying flow conditions.

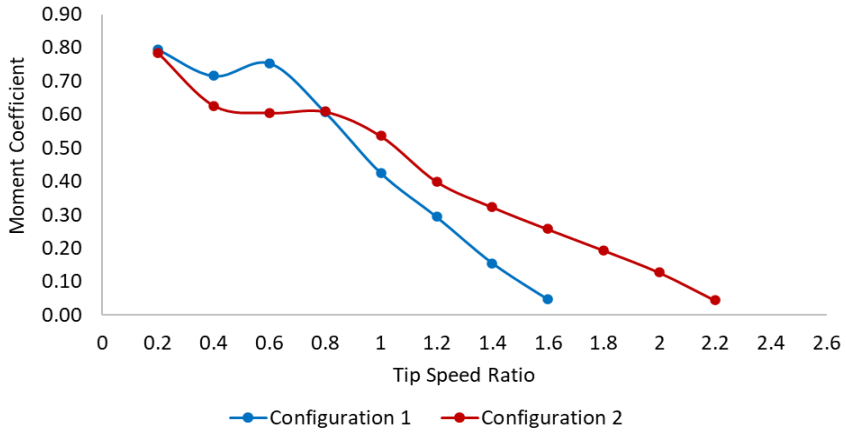

Figure 15. Moment Coefficient of the Fore Turbine as a Function of Tip Speed Ratio for Both Configurations

P-ISSN: 1411-3414
E-ISSN: 2549-9815

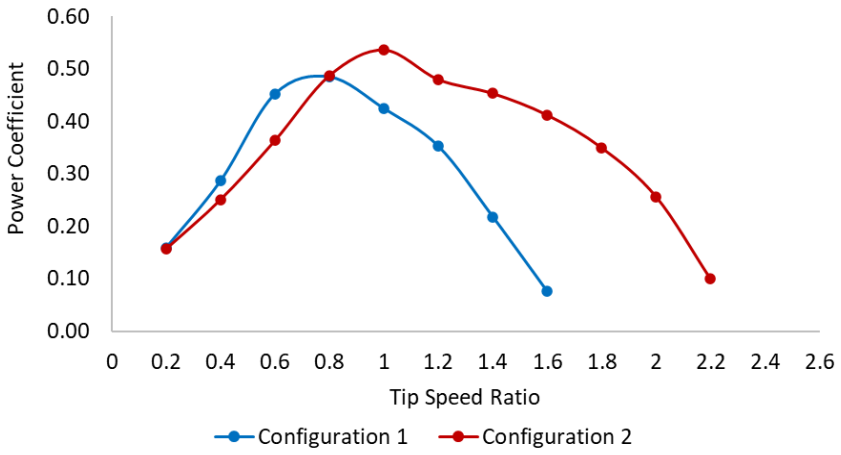

Figure 16. Power Coefficient of the Fore turbine as a Function of Tip Speed Ratio for Both Configurations

3.3.2 Rear Turbine

Figure 17 and Figure 18 illustrate the moment coefficient and power coefficient for both configurations of the rear turbine. In configuration 1, the rear turbine operates within the wake region generated by the fore turbine. The incoming flow that interacts with the rear turbine exhibits relatively low velocity and high turbulence intensity, resulting in a weakened pressure gradient around the blades. Consequently, both the moment and power coefficients remain low at smaller TSR values. Although increasing the TSR partially restores the flow, the wall-induced blockage effect remains significant, thereby limiting the overall performance improvement.

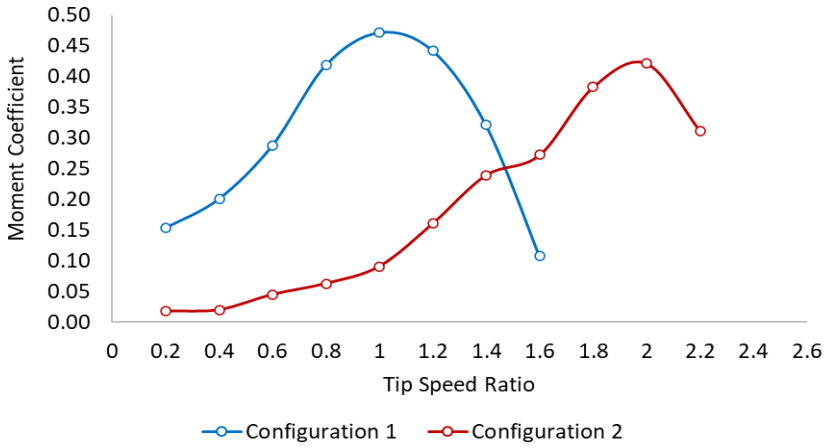

Figure 17. Moment Coefficient of the Rear Turbine as a Function of Tip Speed Ratio for Both Configurations

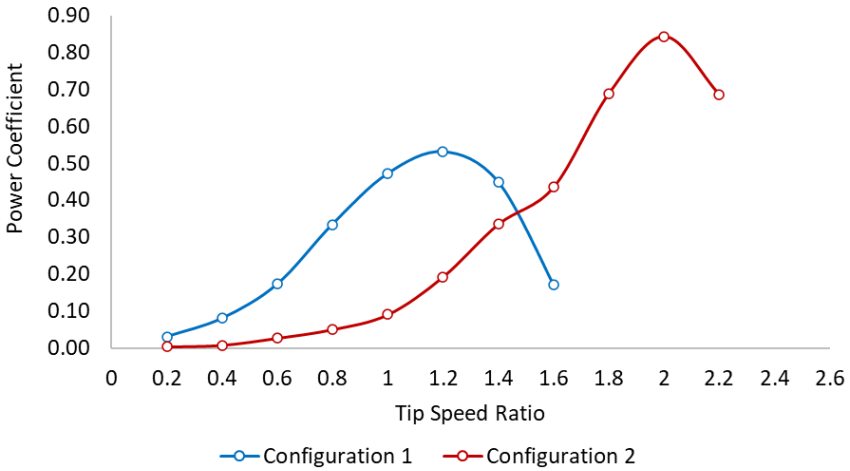

Figure 18. Power Coefficient of the Rear Turbine as a Function of Tip Speed Ratio for Both Configurations

P-ISSN: 1411-3414
E-ISSN: 2549-9815

At configuration 2, the fore turbine generates a more directed flow due to the formation of a nozzle effect between the advancing blade and the wall. As a result, a greater portion of the high-velocity flow is directed toward the rear turbine, allowing it to receive an inflow with higher kinetic energy and a more balanced pressure distribution. This enhances the aerodynamic efficiency of the rear turbine. At higher TSR values, the rear turbine in configuration 2 is able to maintain a relatively stable power coefficient, indicating a more synergistic flow interaction between the two turbines. Furthermore, configuration 2 exhibits a wider operational TSR range, signifying its capability to operate efficiently at relatively higher rotational speeds.

Overall, configuration 1 demonstrates superior performance at lower tip speed ratios (TSR ≤ 1.4), making it more suitable for low-speed operating conditions. Then, configuration 2 performs better at higher TSR values. Therefore, further investigation into the optimal spacing between the fore and rear turbines is necessary to achieve maximum overall system performance.

3.3.3 Velocity and Pressure Contour

The velocity and pressure contour distributions at a tip speed ratio (TSR) of 1.2 for both configurations are presented in Figure 19 and Figure 20. In configuration 1, the fore turbine induces a pronounced downward flow deflection due to the blockage effect caused by the wall. This phenomenon generates a large bubble separation behind the fore turbine and extends the wake region that interacts with the rear turbine. As a result, the rear turbine receives a low-velocity and non-uniform inflow, leading to a weakened pressure gradient around the blades and a subsequent reduction in the generated torque. Such blockage effects are well-documented to degrade downstream turbine performance by increasing velocity deficits and turbulence intensity in the wake region [46]–[49]. Studies confirm that higher blockage ratios intensify these effects, especially at moderate to high tip speed ratios, causing greater energy losses and performance reduction for the rear turbine [46], [47], [49].

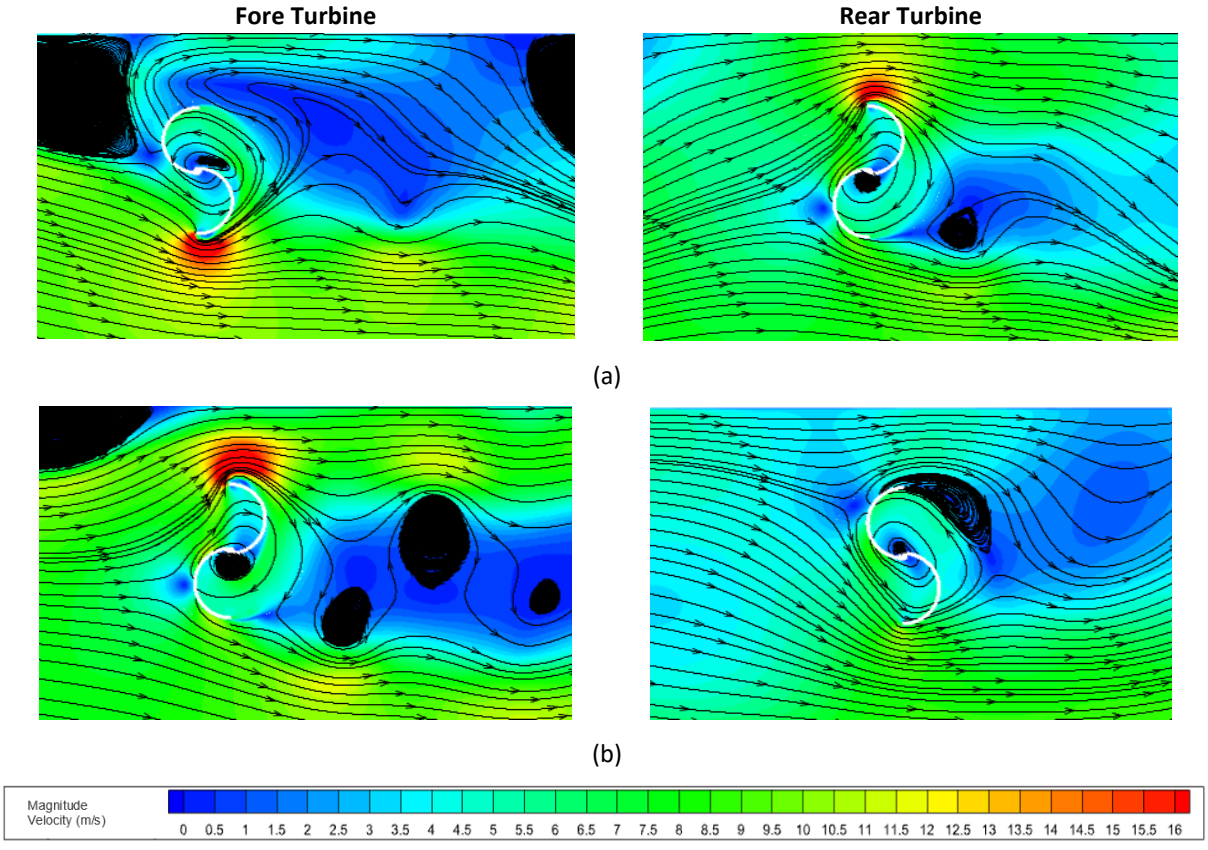

Figure 19. Velocity Contours of the Fore and Rear Turbines at an Azimuth Angle of 90° and TSR = 1.2: a) Configuration 1, b) Configuration 2

In contrast, configuration 2 exhibits a more organized and direct flow pattern, characterized by a strong nozzle effect formed in the narrow gap between the wall and the advancing blade. The high-

P-ISSN: 1411-3414
E-ISSN: 2549-9815

velocity jet emerging from this region accelerates the flow recovery around the rear turbine and shortens the wake region. The pressure distribution becomes more balanced, with a clearer pressure difference between the advancing and returning blade surfaces for both turbines. The pressure distribution becomes more balanced, supporting a clearer pressure difference across the blades and enhancing aerodynamic efficiency [50]–[52]. This indicates a more efficient aerodynamic interaction between the two turbines, promoting a stable flow structure and enhancing energy conversion potential. Enhanced wake mixing and recovery are associated with improved energy conversion and allow for tighter turbine spacing without significant performance loss [50]–[52].

Overall, configuration 1 tends to experience greater energy losses due to the combined effects of blockage and an extended wake region, whereas configuration 2 demonstrates higher aerodynamic efficiency by effectively utilizing the flow acceleration induced by the nozzle effect. Therefore, configuration 2 can be considered more advantageous in terms of flow stability and overall aerodynamic performance.

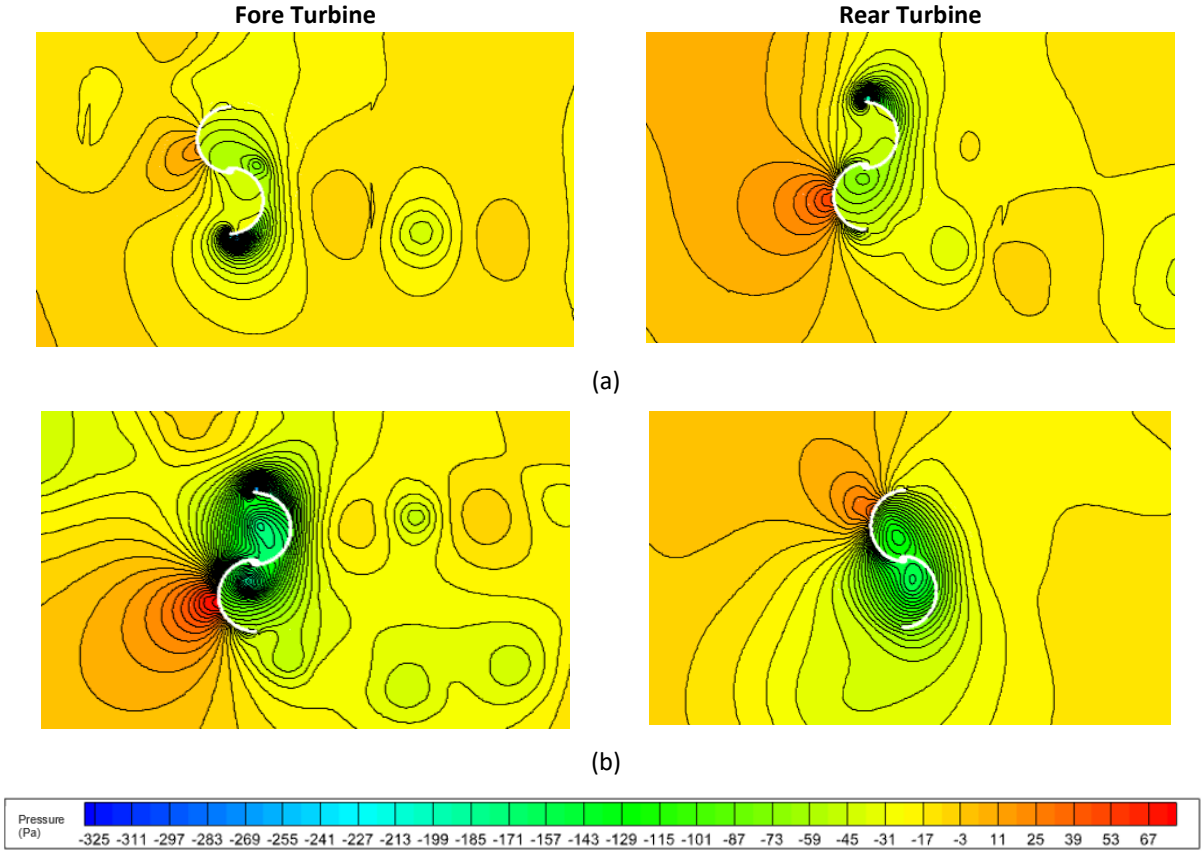

Figure 20. Pressure Contours of the Fore and Rear Turbines at an Azimuth Angle of 90° and TSR = 1.2: a) Configuration 1, b) Configuration 2

4. Conclusion

This study aimed to analyze the effect of the blade orientation of tandem-configured Savonius wind turbines placed adjacent to a wall on turbine performance at a wind velocity of 7 m/s. Two configurations were examined: configuration 1, where the returning blades are positioned adjacent to each other, and configuration 2, where the advancing blades are positioned adjacently. The main findings of this research can be summarized as follows:

- The presence of the wall causes the airflow to deflect away from it, resulting in the formation of a bubble separation near the wall edge. This phenomenon significantly influences the development of low-velocity regions and the blockage effect around the blades, ultimately affecting the turbine's torque and power efficiency.
- For the fore turbine, configuration 2 demonstrates the best performance, producing higher output and a broader operational tip speed ratio range compared to configuration 1.

- At low tip speed ratios (TSR ≤ 1.4), configuration 1 performs more effectively than configuration 2, making it suitable for low-speed operation. Conversely, configuration 2 exhibits superior performance at higher TSR values. Therefore, further investigations are necessary to determine the optimal spacing between the fore and rear turbines to achieve the best overall performance.

The results of this study indicate that blade orientation plays a critical role in governing flow behavior and energy extraction in wall-mounted tandem Savonius turbines. These findings highlight that proper blade–wall positioning is essential for optimizing aerodynamic interaction and energy yield in urban, space-constrained wind installations, and provide valuable guidance for the design and placement of small-scale building-integrated wind systems.

References

[1] W. Y. Wang, M. C. Tsai, and Z. H. Liu, "Wind energy potential in compact urban areas with balconies," *Physics of Fluids*, vol. 37, no. 1, Jan. 2025, doi: 10.1063/5.0243434.

[2] J. Cao, Z. Chen, S. Kong, L. Liu, and R. Wang, "Towards urban wind utilization: The spatial characteristics of wind energy in urban areas," *J Clean Prod*, vol. 450, p. 141981, Apr. 2024, doi: 10.1016/J.JCLEPRO.2024.141981.

[3] H. Hasbiyati, Q. Qanitah, and M. Nuruddin, "PENGEMBANGAN PROTOTIPE TURBIN SEBAGAI PROYEK APLIKASI ENERGI TERBARUKAN," *DINAMIS*, vol. 21, no. 2 Desember, pp. 64–70, Dec. 2024, doi: 10.58839/JD.V21I2.1466.

[4] K. C. S. Kwok and G. Hu, "Wind energy system for buildings in an urban environment," *Journal of Wind Engineering and Industrial Aerodynamics*, vol. 234, p. 105349, Mar. 2023, doi: 10.1016/J.JWEIA.2023.105349.

[5] S. Liu *et al.*, "Advances in urban wind resource development and wind energy harvesters," *Renewable and Sustainable Energy Reviews*, vol. 207, p. 114943, Jan. 2025, doi: 10.1016/J.RSER.2024.114943.

[6] G. Krasniqi, C. Dimitrieska, and S. Lajqi, "Wind Energy Potential in Urban Area: Case Study Prishtina," *International Journal of Technology*, vol. 13, no. 3, pp. 458–472, 2022, doi: 10.14716/IJTECH.V13I3.5323.

[7] Haning Hasbiyati, & Audha Fitrah Aulina. Wind Turbine Research Map: An Overview of Renewable Energy Technology Innovation Trends. *Jurnal Ilmiah Teknik*, *4*(2), 54–71. 2025. https://doi.org/10.56127/juit.v4i2.1992

[8] A. Rezaeiha, H. Montazeri, and B. Blocken, "A framework for preliminary large-scale urban wind energy potential assessment: Roof-mounted wind turbines," *Energy Convers Manag*, vol. 214, p. 112770, Jun. 2020, doi: 10.1016/J.ENCONMAN.2020.112770.

[9] R. K. Reja *et al.*, "A review of the evaluation of urban wind resources: challenges and perspectives," *Energy Build*, vol. 257, p. 111781, Feb. 2022, doi: 10.1016/J.ENBUILD.2021.111781.

[10] Q. Liu, Y. Chen, and W. Cao, "Dual-domain reciprocal learning design for few-shot image classification," *Neural Comput Appl*, 2023, doi: 10.1007/s00521-023-08255-z.

[11] A. V. Diaz, I. H. Moya, J. E. Castellanos, and E. G. Lara, "Optimal Positioning of Small Wind Turbines Into a Building Using On-Site Measurements and Computational Fluid Dynamic Simulation," *J Energy Resour Technol*, vol. 146, no. 8, Aug. 2024, doi: 10.1115/1.4065381.

[12] M. Zabarjad Shiraz, A. Dilimulati, and M. Paraschivoiu, "Wind power potential assessment of roof mounted wind turbines in cities," *Sustain Cities Soc*, vol. 53, p. 101905, Feb. 2020, doi: 10.1016/J.SCS.2019.101905.

[13] K. Wijesooriya, D. Mohotti, C. K. Lee, and P. Mendis, "A technical review of computational fluid dynamics (CFD) applications on wind design of tall buildings and structures: Past, present and future," *Journal of Building Engineering*, vol. 74, p. 106828, Sep. 2023, doi: 10.1016/J.JOBE.2023.106828.

[14] D. P. Sari and K. P. Cho, "Performance Comparison of Different Building Shapes Using a Wind Tunnel and a Computational Model," *Buildings 2022, Vol. 12, Page 144*, vol. 12, no. 2, p. 144, Jan. 2022, doi: 10.3390/BUILDINGS12020144.

[15] H. Hasbiyati and A. F. Aulina, "CFD Simulation of Pipe Joints Using SimScale: Analysis of the Effect of Different Inlet Velocities on Water Fluid Flow," *INVOTEK: Jurnal Inovasi Vokasional dan Teknologi*, vol. 25, no. 1, pp. 23–38, Aug. 2025, doi: 10.24036/INVOTEK.V25I1.1263.

[16] P. Mohai *et al.*, "A hybrid BEM-CFD model for effective numerical siting analyses of wind turbines in the urban environment," *J Phys Conf Ser*, vol. 1037, no. 7, p. 072029, Jun. 2018, doi: 10.1088/1742-6596/1037/7/072029.

[17] M. Slama *et al.*, "Turbine design dependency to turbulence: An experimental study of three scaled tidal turbines," *Ocean Engineering*, vol. 234, p. 109035, Aug. 2021, doi: 10.1016/J.OCEANENG.2021.109035.

[18] S. Gambuzza and B. Ganapathisubramani, "The effects of free-stream turbulence on the performance of a model wind turbine," *Journal of Renewable and Sustainable Energy*, vol. 13, no. 2, Mar. 2021, doi: 10.1063/5.0039168.

[19] A. Vinod and A. Banerjee, "Performance and near-wake characterization of a tidal current turbine in elevated levels of free stream turbulence," *Appl Energy*, vol. 254, p. 113639, Nov. 2019, doi: 10.1016/J.APENERGY.2019.113639.

[20] A. Talamalek, M. C. Runacres, and T. De Troyer, "Effect of Free-Stream Turbulence on the Power Performance and Wake Characteristics of Paired Counter-Rotating Vertical-Axis Wind Turbines," *Wind Energy*, vol. 28, no. 2, p. e2968, Feb. 2025, doi: 10.1002/WE.2968.

[21] B. Belabes and M. Paraschivoiu, "Numerical study of the effect of turbulence intensity on VAWT performance," *Energy*, vol. 233, p. 121139, Oct. 2021, doi: 10.1016/J.ENERGY.2021.121139.

[22] Y. Li, Q. Song, Q. S. Li, D. L. Wang, and X. P. Wu, "Experimental investigation of wind loads on wind turbine blade under various turbulent flows," *Advances in Structural Engineering*, vol. 24, no. 16, pp. 3809–3824, Dec. 2021, doi: 10.1177/13694332211040137.

[23] A. Ducoin, M. S. Shadloo, and S. Roy, "Direct Numerical Simulation of flow instabilities over Savonius style wind turbine blades," *Renew Energy*, vol. 105, pp. 374–385, May 2017, doi: 10.1016/J.RENENE.2016.12.072.

[24] J. Michna and K. Rogowski, "CFD Calculations of Average Flow Parameters around the Rotor of a Savonius Wind Turbine," *Energies 2023, Vol. 16, Page 281*, vol. 16, no. 1, p. 281, Dec. 2022, doi: 10.3390/EN16010281.

[25] H. L. Bai, C. M. Chan, X. M. Zhu, and K. M. Li, "A numerical study on the performance of a Savonius-type vertical-axis wind turbine in a confined long channel," *Renew Energy*, vol. 139, pp. 102–109, Aug. 2019, doi: 10.1016/J.RENENE.2019.02.044.

[26] Z. Mao, G. Yang, T. Zhang, and W. Tian, "Aerodynamic Performance Analysis of a Building-Integrated Savonius Turbine," *Energies 2020, Vol. 13, Page 2636*, vol. 13, no. 10, p. 2636, May 2020, doi: 10.3390/EN13102636.

[27] S. Ōtomo, Y. Tasaka, P. Denissenko, and Y. Murai, "On the rotation of a Savonius turbine at low Reynolds numbers subject to Kolmogorov cascade of turbulence," *Physics of Fluids*, vol. 36, no. 2, Feb. 2024, doi: 10.1063/5.0180939/3261707.

[28] Y. Jooss, R. J. Hearst, and T. Bracchi, "Influence of incoming turbulence and shear on the flow field and performance of a lab-scale roof-mounted vertical axis wind turbine," *Journal of Renewable and Sustainable Energy*, vol. 15, no. 6, p. 63302, Nov. 2023, doi: 10.1063/5.0170059/2920285.

[29] Y. Kurniawan and I. Bagus Dharmawan, "Prototipe Turbin Angin Savonius Variasi Extra Layers dengan Pengujian Real Wind Condition Prototype Savonius Wind Turbine Extra Layers Variation With Experiment Real Wind Condition," 2021.

[30] M. Lundberg, A. Manousidou, J. Solhed, and J. Sundberg, "Two-dimensional Study of Blade Profiles for a Savonius Wind Turbine," 2020. [Online]. Available: http://www.teknat.uu.se/student

[31] A. F. Kaya, A. Acir, and E. Kaya, "Numerical investigation of wind-lens combinations for improving aerodynamic performance of an elliptical-bladed Savonius wind turbine," *Journal of the Brazilian Society of Mechanical Sciences and Engineering*, vol. 45, no. 6, Jun. 2023, doi: 10.1007/s40430-023-04216-8.

[32] M. H. Pranta, M. S. Rabbi, and M. M. Roshid, "A computational study on the aerodynamic performance of modified savonius wind turbine," *Results in Engineering*, vol. 10, Jun. 2021, doi: 10.1016/j.rineng.2021.100237.

[33] H. Saputro, M. E. Purdiatama, D. S. Wijayanto, R. Muslim, and F. A. Munir, "Numerical study of savonius wind turbines performance at Demak coastal area, Indonesia: A comparative study of savonius wind turbines without fin and with fin," in *IOP Conference Series: Earth and Environmental Science*, IOP Publishing Ltd, Mar. 2021. doi: 10.1088/1742-6596/1808/1/012026.

[34] P. A. Setiawan, T. Yuwono, and W. A. Widodo, "Numerical Study of the Stagger Angle Effect of a Circular Cylinder Installed in front of Returning Blade Toward the Vertical Axis Savonius Water Turbine Performance," in *Journal of Physics: Conference Series*, Institute of Physics Publishing, Aug. 2019. doi: 10.1088/1742-6596/1179/1/012107.

[35] S. Shahriare, M. R. Rony, and P. Das, "Enhanced Aerodynamic Performance of Savonius Wind Turbines Through Blade Design Modifications: A CFD Study," *Wind Energy*, vol. 28, no. 8, Aug. 2025, doi: 10.1002/we.70042.

[36] M. Sya, banur Rozaq, R. Romadhon, J. Pradipta, I. N. Haq, and E. Leksono, "Analysis of the Effect of Varying Water Flow Rates on Photovoltaic Module Cooling Systems using CFD (Computational Fluid Dynamics) Simulations," *Jurnal Otomasi Kontrol dan Instrumentasi*, vol. 16, no. 2, pp. 151–161, 2024, doi: 10.5614/joki.2024.16.2.9.

[37] Z. Mu *et al.*, "Study on Aerodynamic Characteristics of a Savonius Wind Turbine with a Modified Blade," *Energies (Basel)*, vol. 15, no. 18, Sep. 2022, doi: 10.3390/en15186661.

[38] E. Nur Fridayana, Y. Setyo Hadiwidodo, D. Satrio, and E. Nensy Irawan, "Studi Model Turbulensi pada Vertical Axis Water Turbine (VAWT) Menggunakan Metode Computational Fluid Dynamics (CFD)," *Syntax Literate: Jurnal Ilmiah Indonesia*, vol. 7, no. 6, 2022.

[39] C. Y. Satriatama, I. Haryanto, and K. Rozi, "SIMULASI DAN ANALISIS AERODINAMIKA TURBIN SAVONIUS," 2025.

[40] G. Sakti and T. Yuwono, "NUMERICAL AND EXPERIMENTAL INVESTIGATION OF THE EFFECT OF A CIRCULAR CYLINDER AS PASSIVE CONTROL ON THE SAVONIUS WIND TURBINE PERFORMANCE," *Journal of Southwest Jiaotong University*, vol. 56, no. 6, pp. 73–93, Dec. 2021, doi: 10.35741/issn.0258-2724.56.6.7.

[41] D. Zulhidayat Noor, H. Mirmanto, A. Anzip, and H. Sasongko, "Influence of Front and Rear Wings on Aerodynamic Forces in a Student Formula Car," *JMES The International Journal of Mechanical Engineering and Sciences*, vol. 8 No.2, pp. 76–83, Sep. 2024, doi: dx.doi.org/10.12962%2Fj25807471.v8i2.21073.

[42] Z. Mao, G. Yang, T. Zhang, and W. Tian, "Aerodynamic performance analysis of a building-integrated Savonius turbine," *Energies (Basel)*, vol. 13, no. 10, May 2020, doi: 10.3390/en13102636.

[43] H. Lu *et al.*, "Aerodynamic performance improvements for a Savonius turbine above a forward-facing step via inclined solar panel: A computational study," *J Clean Prod*, vol. 413, Aug. 2023, doi: 10.1016/j.jclepro.2023.137413.

[44] P. Larin, M. Paraschivoiu, and C. Aygun, "CFD based synergistic analysis of wind turbines for roof mounted integration," *Journal of Wind Engineering and Industrial Aerodynamics*, vol. 156,

pp. 1–13, Sep. 2016, doi: 10.1016/j.jweia.2016.06.007.

[45] E. Fatahian, F. Ismail, M. H. H. Ishak, and W. S. Chang, "Aerodynamic performance improvement of Savonius wind turbine through a passive flow control method using grooved surfaces on a deflector," *Ocean Engineering*, vol. 284, Sep. 2023, doi: 10.1016/j.oceaneng.2023.115282.

[46] M. Kong *et al.*, "Correction of sidewall blockage effect for twin-rotor vertical axis tidal stream turbine subjected to different solidities," *Physics of Fluids*, vol. 37, no. 3, Mar. 2025, doi: 10.1063/5.0263049/3339500.

[47] A. Rezaeiha, I. Kalkman, and B. Blocken, "CFD simulation of a vertical axis wind turbine operating at a moderate tip speed ratio: Guidelines for minimum domain size and azimuthal increment," *Renew Energy*, vol. 107, pp. 373–385, Jul. 2017, doi: 10.1016/J.RENENE.2017.02.006.

[48] B. Gaurier, C. Carlier, G. Germain, G. Pinon, and E. Rivoalen, "Three tidal turbines in interaction: An experimental study of turbulence intensity effects on wakes and turbine performance," *Renew Energy*, vol. 148, pp. 1150–1164, Apr. 2020, doi: 10.1016/J.RENENE.2019.10.006.

[49] A. Eltayesh *et al.*, "Effect of Wind Tunnel Blockage on the Performance of a Horizontal Axis Wind Turbine with Different Blade Number," *Energies 2019, Vol. 12,* vol. 12, no. 10, May 2019, doi: 10.3390/EN12101988.

[50] V. Mendoza, E. Katsidoniotaki, M. Florentiades, J. Dot Fraga, and E. Dyachuk, "Aerodynamic performance of a dual turbine concept characterized by a relatively close distance between rotors," *Wind Energy*, vol. 26, no. 6, pp. 521–537, Jun. 2023, doi: 10.1002/WE.2813.

[51] W. Zhang *et al.*, "Research on Aerodynamic Performance of Asynchronous-Hybrid Dual-Rotor Vertical-Axis Wind Turbines," *Energies 2024, Vol. 17,* vol. 17, no. 17, Sep. 2024, doi: 10.3390/EN17174424.

[52] A. Rezaeiha and D. Micallef, "Wake interactions of two tandem floating offshore wind turbines: CFD analysis using actuator disc model," *Renew Energy*, vol. 179, pp. 859–876, Dec. 2021, doi: 10.1016/J.RENENE.2021.07.087.